

Fabrication of Complex 3D Micro-Scale Scaffolds and Drug Delivery Devices using Dynamic Mask Projection Microstereolithography

¹Jae-Won Choi, ²In-Baek Park, ¹Ryan Wicker, ²Seok-Hee Lee, ³Ho-Chan Kim

¹W.M.Keck Center for 3D Innovation, The University of Texas at El Paso, El Paso, TX 79968

²School of Mechanical Engineering, Pusan National University, San 30 Jangjeon-dong, Geumjeong-gu, Busan 609-735, S. Korea

³School of Mechanical Engineering, Andong National University, 388 Songchun-dong, Andong-si, Gyeongbuk, 760-749, S. Korea

Reviewed, accepted September 10, 2008

Abstract

Microstereolithography (μ SL) technology can fabricate three-dimensional (3D) tissue engineered scaffolds with controlled biochemical and mechanical micro-architectures. A μ SL system for tissue engineering was developed using a Digital Micromirror Device (DMDTM) for dynamic pattern generation and an ultraviolet (UV) lamp filtered at 365 nm for crosslinking the photoreactive polymer solution. The μ SL system was designed with x-y resolution of $\sim 2 \mu\text{m}$ and a vertical (z) resolution of $\sim 1 \mu\text{m}$. To demonstrate the use of μ SL in tissue engineering, poly(propylene fumarate) (PPF) was synthesized with a molecular weight of ~ 1200 Da. The viscosity of the PPF was reduced to ~ 150 cP (at 50°C) by mixing with diethyl fumarate (DEF) in the ratio of 7:3 (w/w). Finally, $\sim 2\%$ (w/w) of (bis(2,4,6-trimethylbenzoyl) phenylphosphine oxide) (BAPO) was added to the solution to serve as a photoinitiator. Cure depth experiments were performed to determine the curing characteristics of the synthesized PPF, and the resulting system and photopolymer were used to construct a variety of 3D porous scaffolds with interconnected pores between 100 and 150 μm and a micro-needle array with height of $\sim 800 \mu\text{m}$ and individual tip diameters of $\sim 20 \mu\text{m}$. SEM and microscope images of the micro-architectures illustrate that the developed μ SL system is a promising technology for producing biodegradable and biocompatible microstructures.

INTRODUCTION

In 1993, microstereolithography (μ SL) technology, which evolved from conventional stereolithography, was suggested by Ikuta and Kirowatari [1] and Takagi and Nakajima [2] for producing micro-scale complex structures. The first type of μ SL machine was based on the vector-based scanning SL method, referred to as line-scan. In 1996, Nakamoto and Yamaguchi [3] suggested a mask-based μ SL system, where entire layers were projected at a single time using a physical mask instead of scanning the surface with a laser beam. In 1997, an LCD (Liquid Crystal Display)-based projection μ SL system was developed by Bertsch *et al.* [4]. In 2001, Bertsch *et al.* [5] enhanced the resolution limitation of the LCD system by

replacing the LCD with a DMDTM (Digital Micromirror Device). In μ SL, the LCDs and DMDs are used as dynamic pattern generators or dynamic masks that create any desired pattern on the resin surface, and thus, these methods are referred to as dynamic mask projection methods as opposed to the scanning method described previously. Since the first μ SL system was suggested, many researchers have developed similar μ SL systems because of the superior capability for producing 3D complex microstructures [6–14].

These μ SL systems can produce implantable scaffolds using photocurable biomaterials that allow these scaffolds to be biodegradable and biocompatible. Biodegradability means that the scaffold has to be chemically and gradually degraded *in vivo*, the scaffold has to be destructed without causing cytotoxicity leaving the desired shape of the regenerated organ or tissue. Biocompatibility also means that the surface of the scaffold has to be chemically compatible such that cells attach to and grown on the scaffold, and it is imperative that the scaffold does not induce any undesired reactions (or immune responses) with neighboring organs or tissues [15]. Fortunately, biodegradable and biocompatible materials can be synthesized for use in μ SL. Cooke *et al.* [16] first demonstrated a poly(propylene fumarate) (PPF) scaffold that was fabricated in a conventional SL system, but the scaffold micro-architecture was limited because of the resolution of the system. Lee *et al.* [17, 18] fabricated porous PPF scaffolds using scanning microstereolithography (μ SL) and conducted a cell study using the fabricated scaffolds. The scaffolds fabricated by Lee *et al.*, although fabricated using μ SL, were of simple shapes and provided no real 3D architectures. As a result, the capability of μ SL to fabricate complex 3D micro-architectures has yet to be fully explored, including examining and optimizing the effects of micro-architectures on cell behavior.

In addition to scaffold fabrication, μ SL systems can produce biocompatible drug delivery devices using the biomaterials. Micro-needles, for example, are drug delivery devices that can be designed and manufactured using μ SL to puncture the skin without pain. The punctured micro-holes in the skin can be utilized as a path for drugs, which has even high molecular weight such as a protein. Many researchers have produced micro-needles using microelectromechanical system (MEMS) and lithography, electro-forming, and molding (LIGA) technologies [19–24], although these micro-needles were also limited on the geometric complexity by the manufacturing technology. By using μ SL, it may now be possible to optimize micro-needle design in terms of puncture force, drug delivery rate, and other factors.

This paper demonstrates development of a DMDTM (Digital Micromirror Device)-based microstereolithography (μ SL) system, PPF synthesis and characterization, and fabrication of 3D micro-scaffolds and micro-needles using commercial photopolymers and PPF. PPF was synthesized using DEF (Diethyl fumarate) and PG (Propylene glycol) along with the hydroquinone and zinc chloride. The DMD-based μ SL was developed with the

lateral resolution of $\sim 2 \mu\text{m}$, and vertical resolution of $\sim 1 \mu\text{m}$. The synthesized PPF was mixed with the DEF to reduce the PPF viscosity for use in the μSL system. In order to characterize PPF/DEF, curing, penetration depth and critical energy studies were performed. Finally, the fabricated microstructures were examined by SEM and optical microscopy to examine the ability of the μSL system to produce complex micro-scaffold and micro-needle geometries. The following sections describe these experiments and their results in more detail.

DYNAMIC MASK PROJECTION MICROSTEREOLITHOGRAPHY

Components and Principle

In microstereolithography (μSL), the fabrication method works in the same fashion as in SL. That is, 3D microstructures can be produced by slicing a 3D model with a computer program, solidifying, and stacking images layer by layer in the system [8]. The achievable resolution in μSL is within $10 \mu\text{m}$, whereas it is several tens microns in conventional SL. There are mainly two types of μSL ; one is scanning-based μSL using a focused laser spot and the other is projection-based μSL using a projected light pattern. In scanning μSL , the laser spot is focused and scanned onto the resin surface using a XY-stage to move the spot instead of galvanometer mirror, which induces a defocusing problem [1, 25]. In projection μSL , an illuminated light is patterned using a high-resolution pattern generator, and projected onto the resin surface. Projecting the entire image onto the surface results in solidifying the entire layer at a time without having to scan the surface [4, 6, 7]. In this work, DMD-based dynamic mask projection μSL was used, which was developed previously [8, 9, 12, 14].

DMD-based dynamic mask projection μSL consists of the light emission subsystem (a lamp, an optical fiber, a filter, and a collimating lens set), the light delivery subsystem (a LightGateTM, a tube lens, and a reflecting mirror), the dynamic pattern generation subsystem (the DMDTM), the image focusing subsystem (a modular focusing unit and an objective lens), and the build subsystem (a Z-stage, a platform, a resin vat, and a hot plate) as shown in Fig. 1 [8, 14].

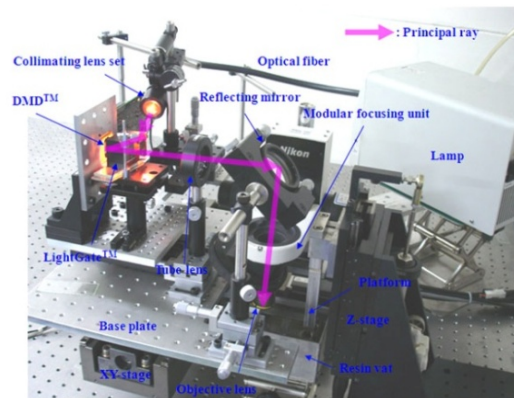


Fig. 1 Developed dynamic mask projection μSL system

In the light emission subsystem, the 200 W mercury lamp (Omniculture S2000™, EXFO, Co., Canada) containing the filter with the wavelength of 365 nm was selected for the light source. The emitted light was delivered via the optical fiber. The collimating lens set, which consists of two convex lenses, was used for collimating the light and illuminating to the DMD™.

In order to make the light delivery subsystem compact, the light path must be reduced. To do this, the LightGate™ (Unaxis Co., USA), which was specially coated for UV light was used as a prism. The LightGate™ reflects the light to DMD™ and transmits the returned pattern to the tube lens. To deliver the patterned light toward the objective lens, the tube lens (Achromat doublet lens, MellesGriot Co., USA) with the focal length of 120 mm and reflecting mirror were used. The tube lens played a role in collimating the patterned light, and was positioned at the focal length from the DMD™. The reflected light from DMD™ was assumed as the source, therefore the light between the tube lens and the objective lens could be collimated.

In the pattern generation subsystem, the DMD™ (DMD Starter Kit, Texas Instruments, USA) was chosen for a dynamic pattern generator. It consists of ~786,000 micromirrors (1024×768), in which each mirror is 13.68 μm along each side, and is independently tilted at ± 12 degrees by an electrostatic force. The principle of generating the light pattern using DMD™ is that the incident light is reflected in two directions according to the mirror tilt angles, and one of the reflected light bundles is the pattern. The bundle of the light reflected at the +12 degrees makes the desired pattern, which is projected on the resin surface through the tube lens and objective lens, whereas the other bundle is projected to a dummy direction. The DMD™ makes a certain pattern by tilting each mirror at ± 12 degrees according to the binary information of each pixel (one pixel is the same as one micromirror), once the binary image is transferred to DMD™ board.

The binary image is generated from the sliced section, which consists of point data with at least one loop. An example of the process for creating the binary image is provided in Fig. 2. In the case where there is more than two loops, there is not any topology relationship between the loops. Therefore, the topology in each section has to be found, and the binary image can be generated according to the number of the loops surrounding a certain loop. That is, each loop is painted black if the number of surrounding loops including itself is odd. Otherwise it is painted white. Each section is painted from the outer loop to the inner loop. In Fig. 2, the loops L_1 , L_2 , L_3 and L_4 have the number of the surrounding loops (including itself) of 1, 2, 2, and 3, respectively. Thus, L_1 is first painted black, then L_2 and L_3 are painted white, and then the L_4 is painted black.

In the image focusing subsystem, two kinds of objective lenses with numerical aperture (N.A.) of 0.13 and 0.3 (CFI Plan Flour, Nikon, Japan) were selectively used as a projection lens. The focal lengths (f_o) of the objective lenses with the N.A. of 0.13 and 0.3

are 50 mm and 20 mm, respectively. The objective lenses were selectively used according to the reduction ratio, which determines the achievable resolution and fabrication volume.

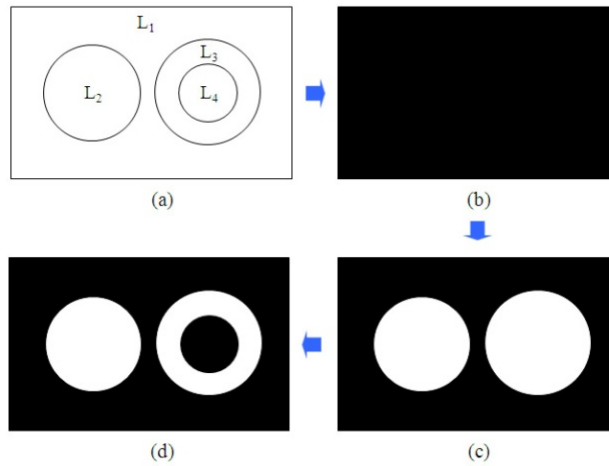


Fig. 2 Binary image generation: (a) loops in a layer, (b) L_1 is painted black (L_1 is the outer most loop), (c) L_2 and L_3 are painted white, and (d) L_4 is painted black (the final binary image)

In addition, the modular focusing unit with the resolution of $1\ \mu\text{m}$ was used for adjusting the distance between the resin surface and objective lens. To simulate and optimize the designed optical system, ZEMAX software was used. The distances between the DMDTM surface and the tube lens (l_{dt}), and the tube lens and the objective lens (l_{to}) as shown in Fig. 3, were optimized. Table 1 shows the original and optimized distances. The magnification can be calculated by the ratio of the distances l_{dt} and f_o by the basic lens equation, because the light between the tube lens and the objective lens was collimated. Therefore, the magnifications using two objective lenses were ~ 0.434 , and ~ 0.174 , so that 1 pixel ($13.68\ \mu\text{m}$) on the DMDTM would represent $\sim 5.9\ \mu\text{m}$ and $\sim 2.4\ \mu\text{m}$, respectively.

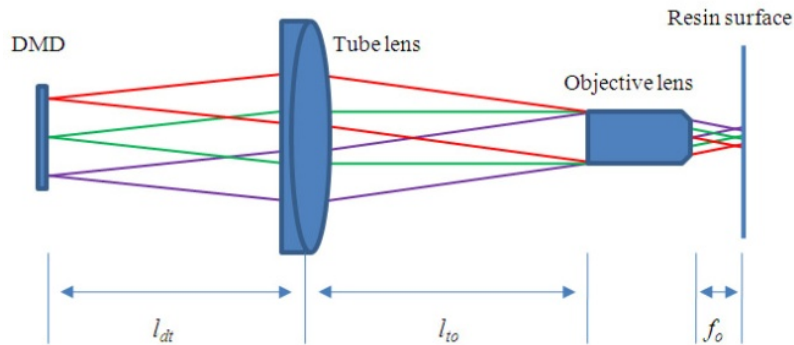


Fig. 3 The distances among DMDTM, tube lens, objective lens, and resin surface

Table 1 The original and optimized distances between the optics

Objective Lens	l_{dt} (mm)		l_{to} (mm)		Magnification (f_o/l_{dt})
	Original distance	Optimized distance	Original distance	Optimized distance	
N.A. 0.13	120	115.2	150	203.3	50/115.2 (0.434)
N.A. 0.3	120	115.2	150	186.5	20/115.2 (0.174)

The build subsystem consisted of a Z-stage with the resolution of 100 nm for stacking, a platform for attaching a substrate, a vat for containing the liquid solution, and a hot plate for controlling the solution temperature. The Z-stage makes a new solution surface with the desired layer thickness by moving downward deeply and then moving upward to the predetermined position. That is, the previously cured layer is immersed deeply so the neighboring solution flows on the top of the layer, and once returned to the predetermined position, the new uncured resin layer is allowed to settle for a certain settling time. The settling time depends on the solution viscosity and can be experimentally determined. Fig. 4 shows the process of refreshing the solution surface. Because the recoating process involves resin flow, the viscosity is a dominant factor in μ SL, and a low viscosity solution is needed to ensure precise layer thicknesses and fast fabrication by reducing settling times.

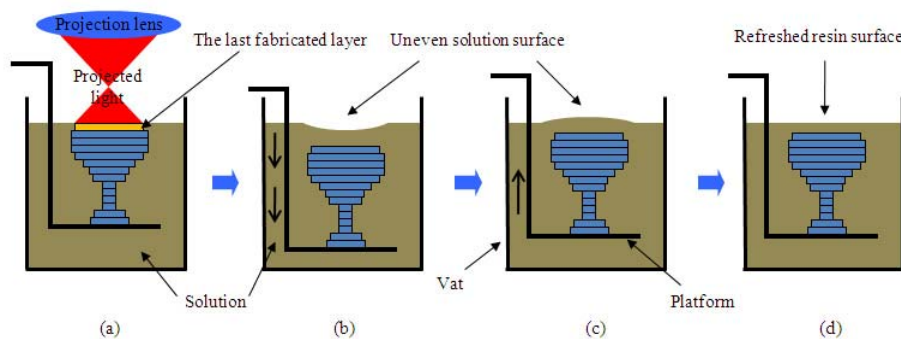


Fig. 4 Building process: (a) irradiation and curing, (b) moving downward deeply for the neighboring solution to flow on the top, (c) moving upward to the desired position, and (d) waiting until the solution surface becomes uniform

PPF/DEF PREPOLYMER

PPF Synthesis

Diethyl fumarate (DEF), propylene glycol (PG), zinc chloride, hydroquinone were purchased from Fisher Scientific Korea (Seoul, S. Korea), and bis(2,4,6-trimethylbenzoyl) phenylphosphine oxide (BAPO) was purchased from Ciba Specialty Korea (Seoul, S. Korea). Poly(propylene fumarate) (PPF) was synthesized with a two-step reaction as previously reported [26–30]. Briefly, DEF and PG were prepared as main components with the molar

ratio of 1 : 3 along with the zinc chloride (0.01 mol) as a catalyst, and hydroquinone (0.002 mol) as a crosslinking inhibitor. In the first reaction, the prepared solution was mixed by an overhead mechanical stirrer, and heated from 100 °C to 150 °C with an increase of 10 °C every 20 minutes under nitrogen. It was maintained for 7 hours (the time is equivalent to ~90 % of reaction) once the temperature reached 150 °C. Diester intermediates as a main product, and ethanol as a byproduct were produced through transesterification at this time. In the second reaction, the solution was maintained at 130 °C under vacuum for 1 hour (the time is equivalent to the predetermined molecular weight of the PPF). PPF as a main product and PG as a byproduct were produced. Synthesized PPF was not purified because it was assumed that any purification process may not affect PPF manufacturability in the μ SL system.

PPF Characterizations

To verify the utilization of synthesized PPF in the developed μ SL system, the viscosity has to be measured and adjusted. If the solution is too viscous (usually the viscosity of the solution in μ SL is maintained below ~200 cP), the solution surface cannot be easily refreshed because of the building process (see Fig. 4). The viscosity of the synthesized PPF was measured using a viscometer (SV-10, AND Co., Japan) and gel permeation chromatography (GPC) was used to measure its molecular weight. The measured viscosity was ~12000 cP at 47 °C as shown in Fig. 5, and the average molecular weight was determined to be ~1200 Da.

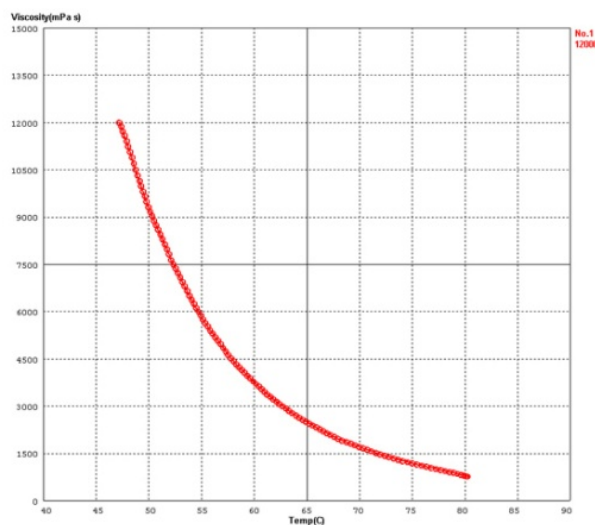


Fig. 5 PPF viscosity according to temperature

PPF/DEF prepolymer preparation

The viscosity of the PPF depends on the time of the second reaction, and the viscosity of the solution has to be modified for μ SL as previously mentioned. Therefore, a diluent is needed

to lower the viscosity of the solution without changing the desired biomaterial properties. DEF, which is a main material for PPF synthesis, was used as the diluent as it has been reported that DEF does not affect the biomaterial properties of PPF. In addition, DEF has a carbon double bond, so it participates in crosslinking [29]. In this work, DEF was added to PPF with the ratio of 3:7 (w/w), and the ratio was obtained from the work of Fisher *et al.* [29]. Fisher *et al.* showed that the mixture of DEF/PPF (~3:7 by weight%), where the molecular weight of the synthesized PPF was 1260 Da, had the highest elastic modulus and the fracture strength. The viscosity of the PPF/DEF as a function of temperature is shown in Fig. 6 and was measured using the same viscometer as above. The PPF/DEF prepolymer was prepared by stirring for 12 hours along with the 2% (w/w) of bis(2,4,6-trimethylbenzoyl) phenylphosphine oxide (BAPO) as a photoinitiator. In Fig. 6, the viscosity of the PPF/DEF represents ~700 cP at room temperature. This viscosity is relatively high compared to desired value of ~200 cP. However, the viscosity of the solution was, logarithmically reduced by elevating the temperature, and the viscosity was ~150 cP at 50 °C. This value is suitable for μ SL [8], so a hot plate was installed under the vat to maintain the temperature of the solution at 50 °C.

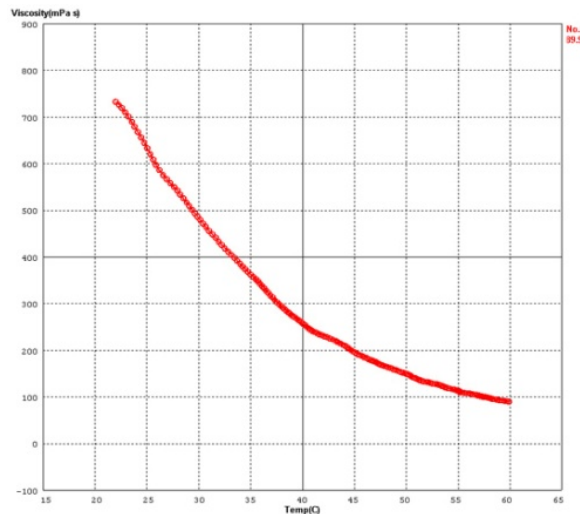


Fig. 6 PPF/DEF viscosity according to temperature

Cure depth experiment

A photocurable solution is crosslinked by connecting a monomer, oligomer or polymer chain, where they have carbon double bonds that can be broken down by a radical. The photons from the projected light break down the photoinitiator into a radical along the penetration direction of the light. The radicals then bond the neighboring monomer, oligomer, or polymer by breaking carbon double bonds. Therefore, in terms of 3D microfabrication, the penetration depth of the light and critical energy at photoinitiation are important and need to

be controlled.

To examine the penetration depth and critical energy, curing depth experiments were conducted using the PPF/DEF prepolymer. The energy delivered on the solution surface (E_{\max}) penetrates into the solution. The energy inside the solution at the depth 'z' ($E(z)$) is defined by Beer-Lambert law as described in Eq. 1 below [31], where D_p is the penetration depth of the solution. By introducing the critical energy (E_c) into the Eq. 1, the curing depth (C_d) can be defined as in Eq. 2, where E_c is the energy at the gel point. The gel point is the point at which solidification begins. Therefore, two important characteristics of the photocurable solution are E_c and D_p . These can be experimentally determined through measuring of the curing depth according to the exposure energy. From the determined values of E_c and D_p , the exposure energy and stacking thickness can be chosen. In addition, it is important to note that the smaller the curing depth, the ability to fabricate down-facing and complex microstructures is improved.

To conduct the curing depth experiment, the curing model as shown in Fig. 7 was used. The curing model consists of posts, which were stacked with 10 layers (1 mm long) with the layer thicknesses of the 100 μm , and crossbeams, which were fabricated in the last layer with the given exposure energy. The irradiance in the developed μSL was 33.8 mW/cm^2 , and the exposure energy was controlled by opening the shutter for 1, 2, 3, 4, and 5 s. The thicknesses of the 4 crossbeams were measured at the center using a microscope (DFC 280, LEICA, Germany).

$$E(z) = E_{\max} \cdot e^{-\frac{z}{D_p}} \quad (1)$$

$$C_d = z(E_{\max}) = D_p \cdot \ln\left(\frac{E_{\max}}{E_c}\right) \quad (2)$$

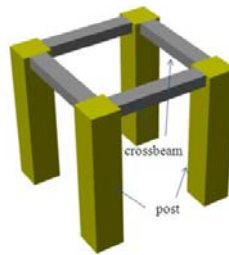


Fig. 7 3D specimen model for curing depth experiment

The specimens for curing characteristics were fabricated as shown in Fig. 8. The crossbeams for 1 s exposure time ($= 33.8 \text{ mJ}/\text{cm}^2$) were not obtained because the thickness of each individual crossbeam was so small that it was broken during rinsing. Fig. 9 represents the cure depth graph by measuring the thickness of the center of the crossbeams. According

to Fig. 11 and Eq. 2, the critical energy and penetration depth were determined to be 32.4 mJ/cm^2 and $78 \text{ }\mu\text{m}$, respectively.

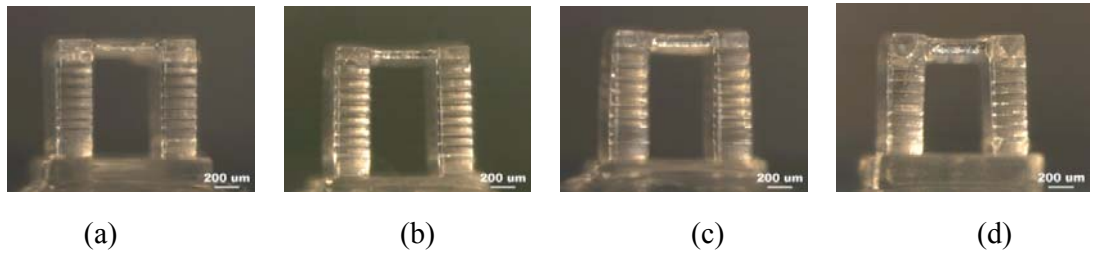


Fig. 8 Fabricated specimens with the crossbeams: (a) 2 s, (b) 3 s, (c) 4 s, and (d) 5 s exposure time

FABRICATED MICROSTRUCTURES

Fabricated microstructure using commercial photopolymers

Commercial photocurable resins are candidates for use in μSL , because many resins are sufficiently reactive with UV light wavelengths used in μSL . Alternatively, commercial monomers along with a photoinitiator can also be designed and used for specific purposes. Using the developed μSL system, several microstructures with complex features were fabricated as shown in Fig. 10. Each microstructure was fabricated using different fabrication conditions and materials as shown in Table 2. Fig. 10 (a) ~ (d) show SEM images of a micro-wineglass, micro-cup, micro-bishop, and micro-springs, respectively. In particular, the XY-stage under the optical system was used for mass production [8, 12], and Fig. 5 (c) shows 9 microstructures in the same build. The achievable feature size was $\sim 30 \text{ }\mu\text{m}$, and the volumes for each are $1 \text{ mm} \times 1 \text{ mm} \times 1.5 \text{ mm}$, $1.95 \text{ mm} \times 1.95 \text{ mm} \times 2.4 \text{ mm}$, $1.7 \text{ mm} \times 1.2 \text{ mm} \times 2.7 \text{ mm}$, and $0.5 \text{ mm} \times 0.5 \text{ mm} \times 1.2 \text{ mm}$ (for one micro-spring), respectively.

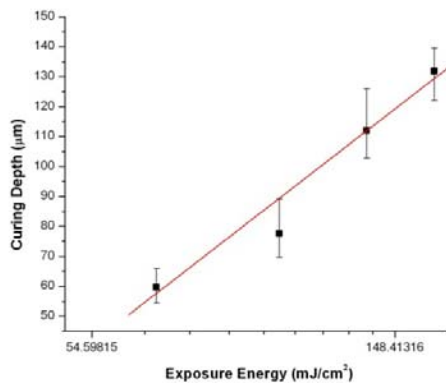


Fig. 9 Cure depth graph according to exposure energy

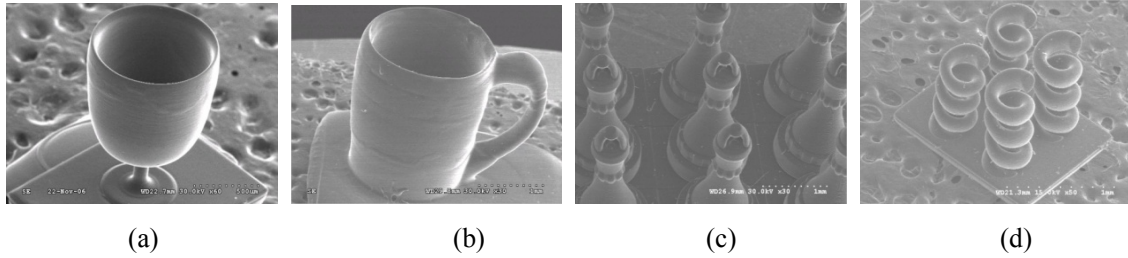


Fig. 10 Fabricated microstructures using the developed μ SL system: (a) micro-wineglass [8], (b) micro-cup [8], (c) micro-bishops [12], and (d) micro-springs [14]

Table 2 Fabrication conditions for the microstructures in Fig. 10

Model	Total layer number	Layer thickness (μm)	Objective lens	Material
(a)	300	5	0.3	SI40 ^a : IBXA ^b = 1 : 1 (w/w)
(b)	200	12	0.13	
(c)	134	20	0.3	IBXA: HDDA ^c : BED ^d = 8 : 1 : 1 (by wt%)
(d)	300	4	0.3	DMPA ^e 5 % (w/w) as a photoinitiator

^aSI40 was purchased from 3D systems (USA), and suitable for conventional SL system

^bIBXA, ^cHDDA, and ^dBED represent Isobornyl acrylate, 1,6-Hexanediol diacrylate, Bisphenol-A-ethoxylated (4) diacrylate, respectively, and purchased from Woorim Chem Tech Co., S. Korea, Miwon Commercial Co., S. Korea, Hannong Chemicals Co., S. Korea, respectively

^eDMPA represents Dimethoxy-2-phenylacetophenone, and purchased from Fisher Scientific Korea, Seoul, S. Korea

Fabricated microstructures using PPF/DEF

Scaffolds were also fabricated as shown in Fig. 11 ~ Fig. 13. Fig. 11 shows a kidney scaffold with a volume of $\sim 1400 \mu\text{m} \times 820 \mu\text{m} \times 700 \mu\text{m}$ and pore size of $\sim 100 \mu\text{m}$. The pores are interconnected as shown in Fig. 11 (c), where micro-CT imaging (Scanco μCT 80) was used to obtain cross-sectional images and internal pore architectures. Fig. 12 and 13 show the cubic and oval scaffold, respectively. The pore sizes are $\sim 85 \mu\text{m}$ and $\sim 145 \mu\text{m}$, respectively, and the volume sizes are $\sim 1280 \mu\text{m} \times 980 \mu\text{m} \times 1320 \mu\text{m}$, and $\sim 1500 \mu\text{m} \times 1030 \mu\text{m} \times 800 \mu\text{m}$, respectively. The scaffolds were fabricated with the thickness of $4 \mu\text{m}$. The micro-CT images in Fig. 12 (c) and Fig. 13 (c) also show good pore interconnectivity. However, the cross-sectional areas of the inner pores in Fig. 13 (c) are smaller than the designed pores. This may be due to some residual PPF/DEF solution that was not completely rinsed out of the pores during the rinsing process.

Using the PPF/DEF solution, 4 micro-needles were fabricated as shown in Fig. 14. The diameter of the micro-needle's tip and base are $\sim 20 \mu\text{m}$ and $\sim 180 \mu\text{m}$, respectively, and the height is $\sim 800 \mu\text{m}$. These images demonstrate the ability of μ SL to effectively fabricate micro-needles that could be used as drug delivery devices.

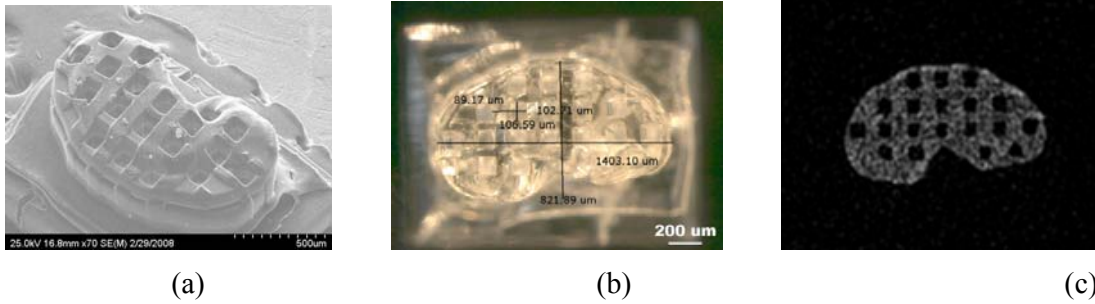


Fig. 11 Fabricated kidney scaffold: (a) SEM image, (b) top view of microscope image and measurement, and (c) cross-section of micro-CT image

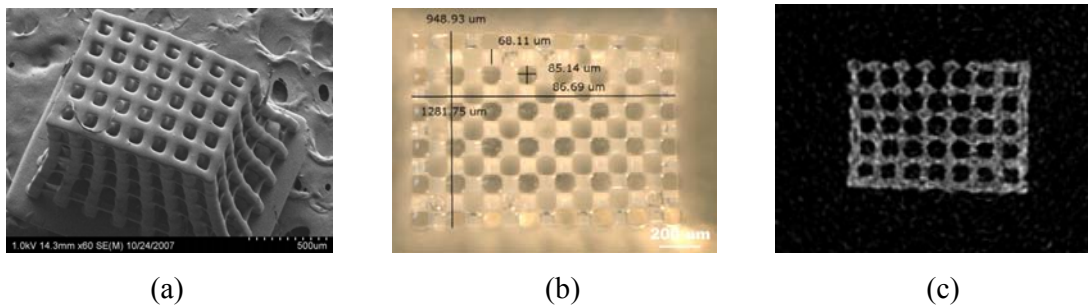


Fig. 12 Fabricated cubic scaffold: (a) SEM image (b) top view of microscope image and measurement, and (c) cross-section of micro-CT image

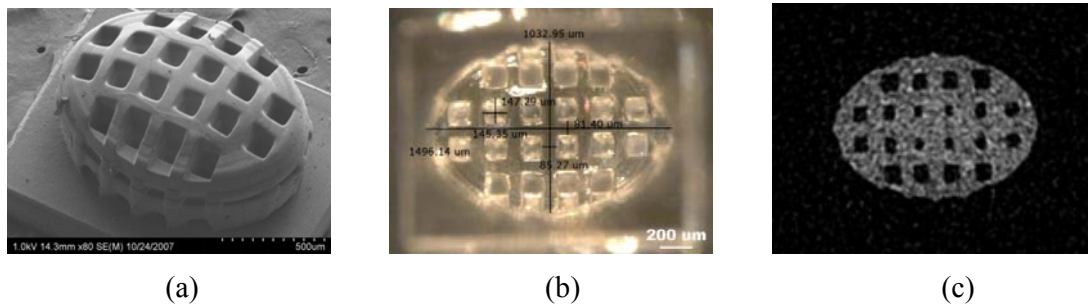


Fig. 13 Fabricated oval scaffold: (a) SEM image (b) top view of microscope image and measurement, and (c) cross-section of micro-CT image

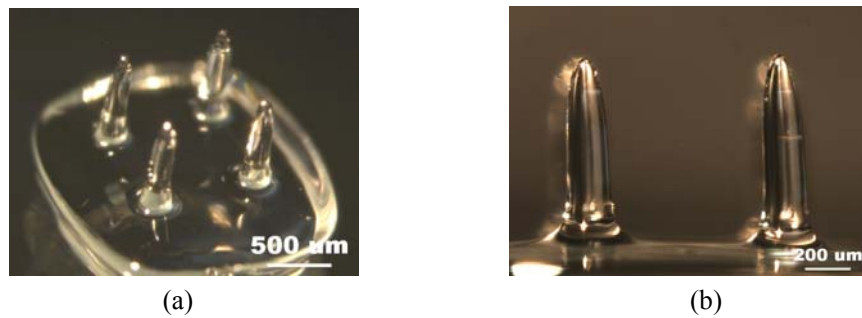


Fig. 14 Fabricated micro-needles: (a) perspective view, and (b) front view

CONCLUSIONS

In this work, 3D micro-scaffolds and micro-needles were fabricated using a previously developed dynamic mask projection μ SL system and the biocompatible polymer PPF. It was confirmed that μ SL has the potential to fabricate complex 3D micro-scale structures with interconnecting pores out of a biopolymer. The synthesized PPF was too viscous to be used in the μ SL system, so the viscosity was reduced by adding DEF. Using the PPF/DEF prepolymer and the developed μ SL system, a curing experiment was conducted to determine the critical energy and penetration depth for the solution. The ability of the system to fabricate complex 3D micro-scaffolds was demonstrated by showing various scaffold geometries with interconnecting pores. The fabricated micro-scaffolds were observed using SEM and optical microscopy, and the cross-sections were investigated using a micro-CT imaging system. In addition to micro-scaffold fabrication, micro-needles were fabricated to demonstrate the ability of μ SL to fabricate biocompatible drug delivery devices. Based on these results, it is concluded that the developed μ SL system and the use of PPF show promise for fabricating micro-scaffolds and drug delivery devices with controlled micro-architectures.

ACKNOWLEDGEMENTS

This work was supported by grant No. R01-2004-000-10507-0 from the Basic Program of the Korea Science & Engineering Foundation, the Mr. and Mrs. MacIntosh Murchison Chair I in Engineering endowment at the University of Texas at El Paso (UTEP), and a research contract from the U.S. Army Space and Missile Defense Command and the Homeland Protection Institute to the Center for Defense Systems Research at UTEP. The findings and opinions presented in this paper are those of the authors and do not necessarily reflect those of the sponsors of this research.

REFERENCES

- [1] Ikuta K., and Kirowatari, K., "Real three dimensional micro fabrication using stereo lithography and metal molding," *Proceedings of 6th IEEE Workshop on Micro Electro Mechanical Systems (MEMS'93)*, New York, NY, 1993, pp. 42~47.
- [2] Takagi, T., and Nakajima, N., "Photoforming applied to fine machining," *Proceedings of 4th International Symposium on Micro Machine and Human Science (MHS'93)*, 1993, pp. 173~178.
- [3] Nakamoto, T., and Yamaguchi, K., "Consideration on the producing of high aspect ratio micro parts using UV sensitive photopolymer," *Proceedings of 7th International Symposium on Micro Machine and Human Science*, 1996, pp. 53~58.
- [4] Bertsch, A., Zissi, S., Jezequel, J.Y., Corbel, S., and Andre, J.C., "Microstereophotolithography using a liquid crystal display as dynamic mask-generator," *Microsystem Technologies*, Vol. 3, No. 2, 1997, pp. 42~47.

- [5] Bertsch, A., Zissi, S., Jezequel, J.Y., Corbel, S. and Andre, J.C., "Microstereolithography: concepts and applications," *Proceedings of 8th IEEE International conference on Emerging Technologies and Factory Automation*, 2001, pp. 289~298.
- [6] Bertsch, A., Jiguet, S., and Renaud, P., "Microfabrication of ceramic components by microstereolithography," *Journal of Micromechanics and Microengineering*, Vol. 14, 2004, pp. 197~203.
- [7] Sun, C., Fang, N., Wu, D.M., and Zhang, X., "Projection micro-stereolithography using digital micro-mirror dynamic mask," *Sensors and Actuators A: Physical*, Vol. 121 No. 1, 2005, pp. 113~120.
- [8] Choi, J.W., *Development of Projection-based Microstereolithography Apparatus Adapted to Large Surface and Microstructure Fabrication for Human Body Application*, Ph. D. Dissertation, Pusan National University, Busan, S. Korea., 2007.
- [9] Choi, J.W., Ha, Y.M., Lee, S.H. and Choi, K.H., "Design of microstereolithography system based on dynamic image projection for fabrication of three-dimensional microstructures," *Journal of Mechanical Science and Technology*, Vol. 20, No. 12, 2006, pp. 2094~2104.
- [10] Choi, J.W., Ha, Y.M., Won, M.H., Choi, K.H, and Lee, S.H., "Fabrication of 3-Dimensional Microstructures using Dynamic Image Projection," *Proceedings of International Conference on Precision Engineering and Micro/Nano Technology in Asia (ASPEN 2005)*, Shenzhen, China, 2005, pp. 472~476.
- [11] Limaye, A.S., and Rosen, D.W., "Process planning method for mask projection micro-stereolithography," *Rapid Prototyping Journal*, Vol. 13, No. 2, 2007, pp. 76~84.
- [12] Ha, Y.M., Choi, J.W., and Lee, S.H., "Mass production of 3-D microstructures using projection microstereolithography," *Journal of Mechanical Science and Technology*, Vol. 22 No. 3, 2008, pp. 514~521.
- [13] Han, L.H., Mapili, G., Chen, S., and Roy, K., "Projection microfabrication of three-dimensional scaffolds for tissue engineering," *Journal of Manufacturing Science and Engineering*, Vol. 130, No. 2, 2008, pp. 021005-1~4.
- [14] Choi, J.W., Wicker, R.B., Cho, S.H., Ha, C.S., and Lee, S.H., "Cure depth control for complex 3D microstructure fabrication in dynamic mask projection microstereolithography," *Rapid Prototyping Journal*, submitted in May, 2008.
- [15] Yang, S., Leong, K.F., Du, Z., and Chua, C.K., "The Design of Scaffolds for Use in Tissue Engineering. Part I. Traditional Factors," *Tissue Engineering*, Vol. 7, No. 6, 2001, pp. 679~689.
- [16] Cooke, M.N., Fisher, J.P., Dean, D., Rimnac, C., and Mikos, A.G., "Use of Stereolithography to Manufacture Critical-sized 3D biodegradable Scaffolds for Bone Ingrowth," *Journal of Biomedical Materials Research Part B: Applied Biomaterials*, Vol. 64B, 2002, pp. 65~69.

- [17] Lee, J.W., Lan, P.X., Kim, B., Lim, G., and Cho, D.W., "3D scaffold fabrication with PPF-DEF using micro-stereolithography," *Microelectronic Engineering*, Vol. 84, 2007, pp. 1702~1705.
- [18] Lee, J.W., Lan, P.X., Kim, B., Lim, G., and Cho, D.W., "Fabrication and characteristic analysis of a poly(propylene fumarate) scaffold using micro-stereolithography technology," *Journal of Biomedical Materials Research Part B: Applied Biomaterials*, Published Online March 11 2008.
- [19] Henry, S., McAllister, D.V., Allen, M.G., and Prausnitz, M.R. "Microfabricated Microneedles: A Novel Approach to Transdermal Drug Delivery," *Journal of Pharmaceutical Sciences*, Vol. 87, No. 8, 1998, pp. 922~925.
- [20] Davis, S.P., Allen, M.G., and Prausnitz, M.R., "The Mechanics of Microneedles," *Proceedings of the Second Joint EMBS/BMES Conference*, Houston, TX, USA, 2002, pp. 498~499.
- [21] Davis, S.P., *Hollow Microneedles for Molecular Transport Across Skin*, Ph. D. Dissertation, Georgia Institute of Technology, Atlanta, GA, 2003.
- [22] Davis, S.P., Landis, B.J., Adams, Z.H., Allen, M.G., and Prausnitz, M.R., "Insertion of microneedles into skin: measurement and prediction of insertion force and needle fracture force," *Journal of Biomechanics*, Vol. 37, 2004, pp. 1155~1163.
- [23] Park, J.H., Allen, M.G., and Prausnitz, M.R., "Biodegradable polymer microneedles: fabrication, mechanics and Transdermal drug delivery," *Proceedings of the 26th Annual International Conference of the IEEE EMBS*, San Francisco, CA, 2004, pp. 2654~2657.
- [24] Park, J.H., Allen, M.G., and Prausnitz, M.R., "Biodegradable polymer microneedles: Fabrication, mechanics and Transdermal drug delivery," *Journal of Controlled Release*, Vol. 104, 2005, pp. 51~66.
- [25] Varadan, V.K., Jiang, X., and Varadan, V.V., *Microstereolithography and Other Fabrication Techniques for 3D MEMS*, John Wiley & Sons Ltd., 2001.
- [26] Peter, S.J., Kim, P., Yasko, A.W., Yaszemski, M.J., and Mikos, A.G., "Crosslinking characteristics of an injectable poly(propylene fumarate)/ ϵ -tricalcium phosphate paste and mechanical properties of the crosslinked composite for use as a biodegradable bone cement," *Journal of Biomedical Materials Research*, Vol. 44, 1999, pp. 314~321.
- [27] Fisher, J.P., Holland, T.A., Dean, D., Engel, P.S., and Mikos, A.G., "Synthesis and properties of photocross-linked poly(propylene fumarate) scaffolds," *Journal of Biomaterials Science Polymer Edition*, Vol. 12, No. 6, 2001, pp. 673~687.
- [28] Shung, A.K., Timmer, M.D., Jo, S., Engel, P.S., and Mikos, A.G., "Kinetics of poly(propylene fumarate) synthesis by step polymerization of diethyl fumarate and propylene glycol using zinc chloride as a catalyst," *Journal of Biomaterials Science Polymer Edition*, Vol. 13, No. 1, 2002, pp. 95~108.
- [29] Fisher, J.P., Vehof, J.W.M., Dean, D., Waerden, J.P., Holland, T.A., Mikos, A.G., and

Jansen, J.A., "Soft and hard tissue response to photocrosslinked poly(propylene fumarate) scaffolds in a rabbit model," *Journal of Biomedical Materials Research*, Vol. 59, 2002, 547~556.

[30] Fisher, J.P., Dean, D., and Mikos, A.G., "Photocrosslinking characteristics and mechanical properties of diethyl fumarate/poly(propylene fumarate) biomaterials," *Biomaterials*, Vol. 23, 2002, pp. 4333~4343.

[31] Jacobs, P.F., *Rapid Prototyping and Manufacturing: Fundamentals of Stereolithography*, Society of Manufacturing Engineers, 1993.